SCIENTIFIC REPORTS

OPEN

# Yttrium Copper Titanate as a Highly Efficient Electrocatalyst for Oxygen Reduction Reaction in Fuel Cells, Synthesized via Ultrafast Automatic Flame Technique

Received: 20 April 2017
Accepted: 27 July 2017
Published online: 24 August 2017

Laxman Singh[1], Uday Pratap Azad[2], Satendra Pal Singh[3], Vellaichamy Ganesan[2], U. S. Rai[2] & Youngil Lee[1]

**Replacing platinum (Pt) metal-based electrocatalysts used in the oxygen reduction reaction (ORR) in fuel cells is an important research topic due to the high cost and scarcity of Pt, which have restricted the commercialization of these clean-energy technologies. The $ABO_3$-type perovskite family of an $ACu_3Ti_4O_{12}$ (A = Ca, Y, Bi, and La) polycrystalline material can serve as an alternative electrocatalyst for the ORR in terms of low-cost, activity, and stability. These perovskite materials may be considered the next generation electro-catalyst for the ORR because of their photocatalytic activity and physical and chemical properties capable of containing a wide range of A- and B-site metals. This paper reports the ORR activity of a new $Y_{2/3}Cu_3Ti_4O_{12}$ perovskite, synthesized via a rapid and facile automatic flame synthesis technique using rotating disk electrode (RDE) measurements. $Y_{2/3}Cu_3Ti_4O_{12}$/C has superior ORR activity, stability, and durability compared to commercial Pt/C. The results presented in this article will provide the future perspectives to research based on $ACu_3Ti_4O_{12}$ (A = Ca, Y, Bi, Sm, Cd, and La) perovskite as the next generation electro-catalyst for the ORR in various electrochemical devices, such as fuel cells, metal–air batteries, and electrolysis.**

Fuel cells (FCs) are a new power source via the direct conversion of hydrogen to electricity as a potential replacement for Li-ion batteries systems in terms of safety, high efficiency, renewable sources, and environmental friendliness[1]. The major obstacle to the commercialization of fuel cells is the high cost, poor stability, and slow kinetics of the oxygen reduction reaction (ORR) of platinum and platinum-based electrocatalysts in fuel-cell electrodes[2]. Thus far, the best electrocatalysts for the ORR of the cathode are carbon-supported Pt and/or its composites[3–8]. High cost and scarcity of platinum requires either use of noble metal with an increased efficiency or the utilization of non-precious electrocatalysts for commercialization on a large scale. In addition, Pt-based electrocatalysts suffer from methanol crossover and CO poisoning[9]. The ORR is not only an essential electrochemical process in fuel cells, but is also required for other electrochemical technologies, such as metal-air batteries and water electrolysis[10]. The ORR takes place through multiple electron transfer in alkaline media. Depending on the nature and electrocatalytic activity of the catalysts, the ORR in alkaline media can occur either via a two electron process to produce $HO_2^-$ or a four electron process to produce $OH^-$ ($O_2 + 2H_2O + 4e^- \rightarrow 4OH^-$)[11]. A high ORR overpotential has been the main obstacle to making these technologies viable. Therefore, major efforts have been made to discover cost-effective and efficient ORR catalysts in traditional aqueous media. A general model of the oxygen reduction kinetics in porous electrodes must include oxygen diffusion, oxygen adsorption, or surface reaction on the active sites of the catalyst, charge transfer, and the diffusion of products[12]. $ABO_3$ type perovskite oxides, particularly $ACu_3Ti_4O_{12}$ (A = Ca, La, Bi, Sm, Cd, and Y), have great potential as low cost, high stability, and better kinetics electro-catalyst and may be considered the next generation electro-catalyst for the ORR because of

[1]Department of Chemistry, University of Ulsan, 93 Daehak-ro Nam-gu, Ulsan, 44610, Republic of Korea. [2]Department of Chemistry, Institute of Science, Banaras Hindu University, Varanasi, 221005, Uttar Pradesh, India. [3]Faculty of Nanotechnology and Advanced Materials Engineering, Sejong University, Seoul, 05006, Republic of Korea. Correspondence and requests for materials should be addressed to Y.L. (email: nmryil@ulsan.ac.kr)

their photocatalytic activity and physical and chemical properties capable of containing a wide variety of A- and B-site metals. These oxide materials have been studied extensively towards a wide range of applications, such as microelectronics, ceramic capacitors, dynamic random-access memory, transducers, microwave device applications, and other electronic devices[13,14]. Currently, the ORR activity of perovskite electrocatalysts has attracted considerable attention[15–18]. The ORR activity of various perovskite materials proceeds through four electron transfer. Different hypothesis for the ORR activity of the perovskite materials have been proposed. Bockris *et al.*[19] suggested that the ORR activity is accompanied by the presence of transition metal d-electrons and the strength of the M-OH bond during the rate determining steps. Suntivich *et al.*[20] reported that the "activity descriptor" governing the ORR activity in transition metal oxides is determined by the extent of σ*-anti bonding ($e_g$) orbital filling of the metal ions on the surface. Matsumoto *et al.*[21] proposed the formation of a σ* bond. The high ORR activity is related to the higher oxidation state of transition metal cations. Until now, the proposed mechanisms are still persisting, which govern the ORR activity in perovskite materials. Various forms of graphene and its nano-composite with metal oxide/metal nanoparticles have been used extensively for FCs. Very few studies have examined the direct use of perovskite and ceramic-based materials for the ORR in FC. Yagi *et al.*[22] showed that the covalent bonding network in the A ($Cu^{2+}$) and B site ($Fe^{4+}$) metal cations improves the structural stability of $CaCu_3Fe_4O_{12}$ increasing the highly active long-life catalysts for the oxygen evolution reaction. Chen *et al.*[23] reported the enhanced reduction of the oxygen catalytic activity of platinized graphene/ceramics due to the better structural stability supported by the ceramic particles. Mathur *et al.*[24] found the enhanced electrocatalytic performance of $Fe_2O_3$ nanoparticles supported on $CaCu_3Ti_4O_{12}$. In view of the above considerations, $ACu_3Ti_4O_{12}$ perovskites have great potential towards the ORR activity and photocatalytic activity, which will provide the next generation electrocatalyst.

$Y_{2/3}Cu_3Ti_4O_{12}$ (YCTO) is an isostructural material of $CaCu_3Ti_4O_{12}$, but still remains relatively unexplored compared to other $ACu_3Ti_4O_{12}$ (A = Ca, La, and Bi). $CaCu_3Ti_4O_{12}$ has already been established as an advanced perovskite compound for visible light active photocatalyst[25,26]. The complex covalent bonding network in $CaCu_3Ti_4O_{12}$ demonstrates the excellent photocatalytic properties for the next generation photocatalyst and provides the foundation of the isostructural perovskites (YCTO) as a promising material for the electrocatalyst. The motivation of this work was to study the ORR activity of the new $Y_{2/3}Cu_3Ti_4O_{12}$ perovskite via rotating disk electrode (RDE) measurements[27] as well as to establish the rapid and facile synthesis of this material (see supporting information S1). $Y_{2/3}Cu_3Ti_4O_{12}$ is a cubic double-perovskite with $Y^{+3}$ and $Cu^{+2}$ on the A site and $Ti^{+4}$ on the B site. Both cations on the A and B sites in the crystal lattice allow considerable control of the band structure, which plays a significant role in the catalytic activity in perovskite materials. To the best of the authors' knowledge, there is no report on the direct use of $ACu_3Ti_4O_{12}$-based perovskite for the ORR in FC. Moreover, a direct transition of 1.8 eV for the visible light absorption of the YCTO ceramic has never been reported, but has great potential as the next generation ORR catalyst and as a photocatalyst.

## Results

**Synthesis of $Y_{2/3}Cu_3Ti_4O_{12}$.** $Y_{2/3}Cu_3Ti_4O_{12}$ perovskite was synthesized via rapid automatic flame synthesis. Supplementary information S1 highlights the merit of the current synthesis procedure over the other reported fabrication procedures for pristine $Y_{2/3}Cu_3Ti_4O_{12}$. Figure 1 presents a schematic diagram of the experimental procedure of automatic flame synthesis. The video and photographs during the occurrence of auto flame synthesis reaction under open air conditions is also available in the supplementary information S2 and S3.

Figure 2(a) shows the simultaneous TG and DSC curves during the thermal decomposition process of the auto flame-synthesized YCTO precursor powder. As shown by the TG curve, the total weight loss is approximately 5.76%. The loss of a very small weight of precursor due to the formation of crystalline phases of metal oxides (see supplementary information Fig. S1) highlights the low probability of the presence of excess organic components after the flame reaction, which is the reason to be required only one sintering step for producing a perovskite phase. The thermal decomposition process could be divided into two steps. The first step has a very small weight loss due to the evaporation of residual water and organic solvents at temperatures below 430 °C. In the second step, weight loss occurs in the temperature range of 430–850 °C accompanied by the decomposition of metal nitrates/organic groups. Above 850 °C, there is almost no weight loss in the TG curve corresponding to the endothermic peak at 848 °C, which was observed in the DSC curve. The absence of a peak in the TG curve beyond 850 °C, is also supported by DSC analysis, which confirms the formation of a YCTO perovskite phase due to a combination of crystalline oxides with solid $TiO_2$ after 850 °C.

**Structural and microstructural analyses of auto flame synthesized $Y_{2/3}Cu_3Ti_4O_{12}$.** A Rietveld refinement is also required to determine the actual structure of the auto flame synthesized YCTO powder for an approximate model structure. The full-pattern Rietveld refinement was carried out using the Fullprof program[28]. The structural parameters reported by Wong-Ng *et al.*[29] were taken as the initial model for the refinement. In the refinements, a Pseudo-Voigt function and 6$^{th}$ coefficient polynomials were used to define the profile shape and the background, respectively. Figure 2(b) shows the results of the Rietveld refinement, which is well matched between the observed and experimental data to ensure a single cubic perovskite phase. The refined lattice parameter in the present case was 7.37743 Å[29], which is very close to that of a previous report, 7.37757 Å[29].

The formation of a single cubic perovskite phase of an auto flame-synthesized YCTO powder was analyzed further with those obtained by Fourier transform infrared (FT-IR) and Raman spectroscopy, as shown in Fig. 2(c) and (d). The main FT-IR absorption peaks were found at 576, 528, and 446 $cm^{-1}$, which were assigned to the absorption regions of the Ti ion ascribed to $\nu_{Ti-O}$ (653–550 $cm^{-1}$) and $\nu_{Ti-O-Ti}$ (495–436 $cm^{-1}$) as shown in Fig. 2(c)[30]. Therefore, the main resonance absorptions are in good agreement with those of a structurally similar CCTO perovskite[31].

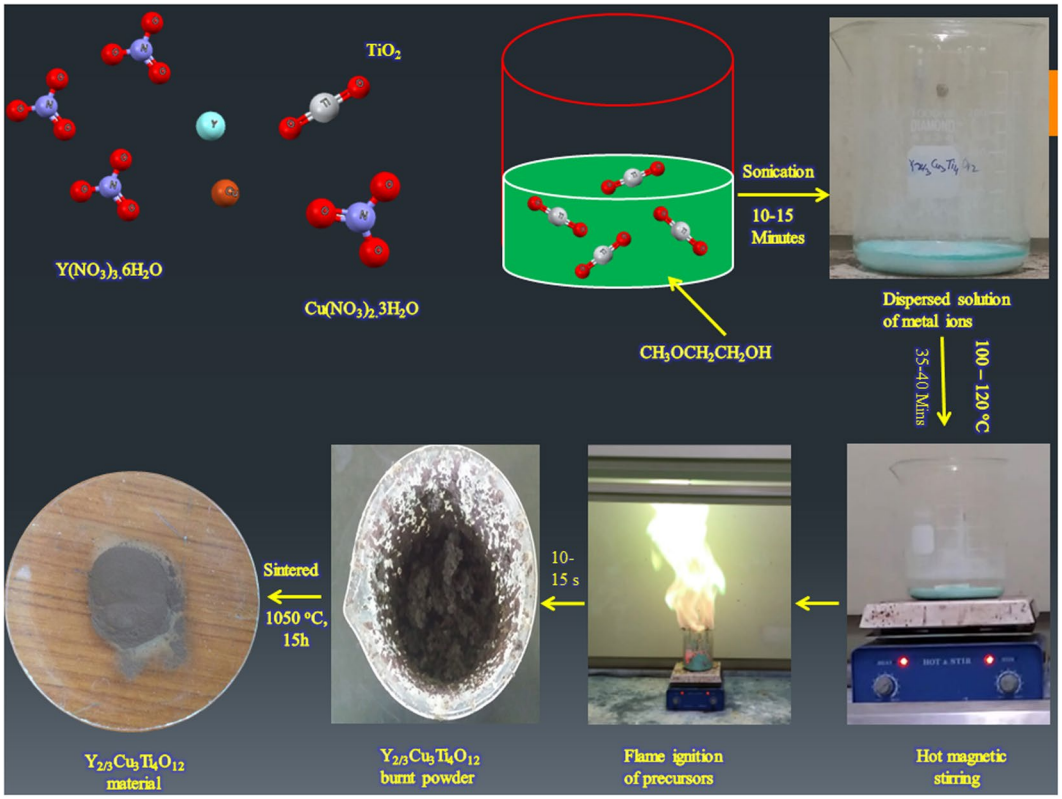


**Figure 1.** Schematic diagram of the flame synthesis procedure to obtain $Y_{2/3}Cu_3Ti_4O_{12}$.

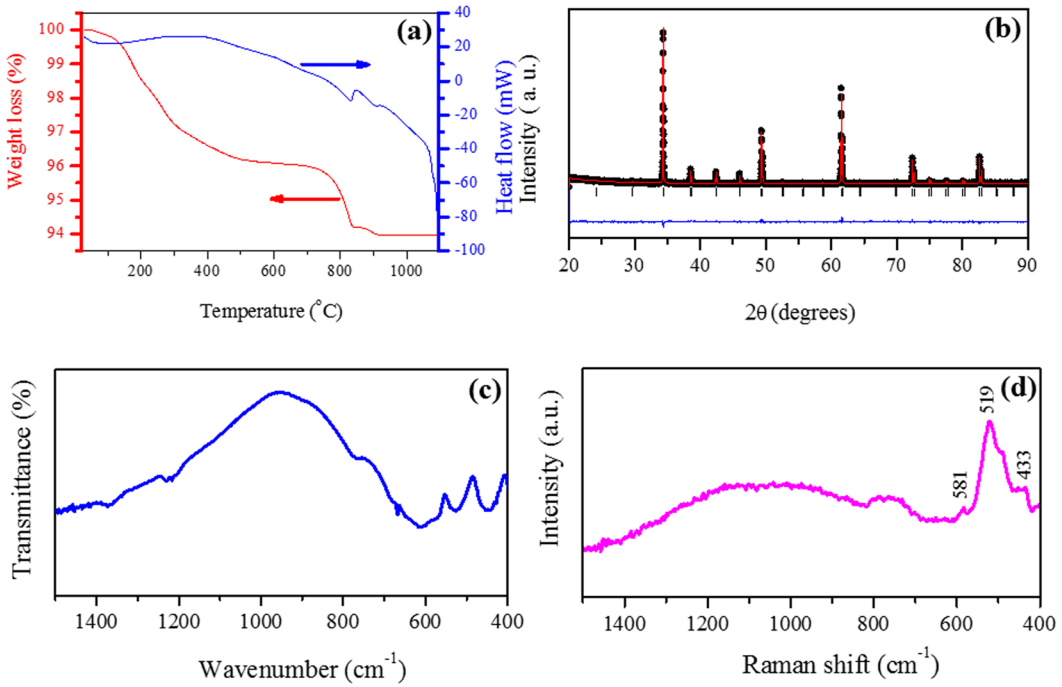


**Figure 2.** (**a**) TGA/DSC curves for the precursor powder of $Y_{2/3}Cu_3Ti_4O_{12}$ and (**b**) Rietveld refinement fit of $Y_{2/3}Cu_3Ti_4O_{12}$. Black dot, red line, black vertical bars and blue line in the figure represent the experimental data, fitted curve, Bragg's reflections and difference profile respectively. (**c**) Fourier transforms infrared and (**d**) Raman spectra of the precursor powders heat treated at 1050 °C for 15 hrs.

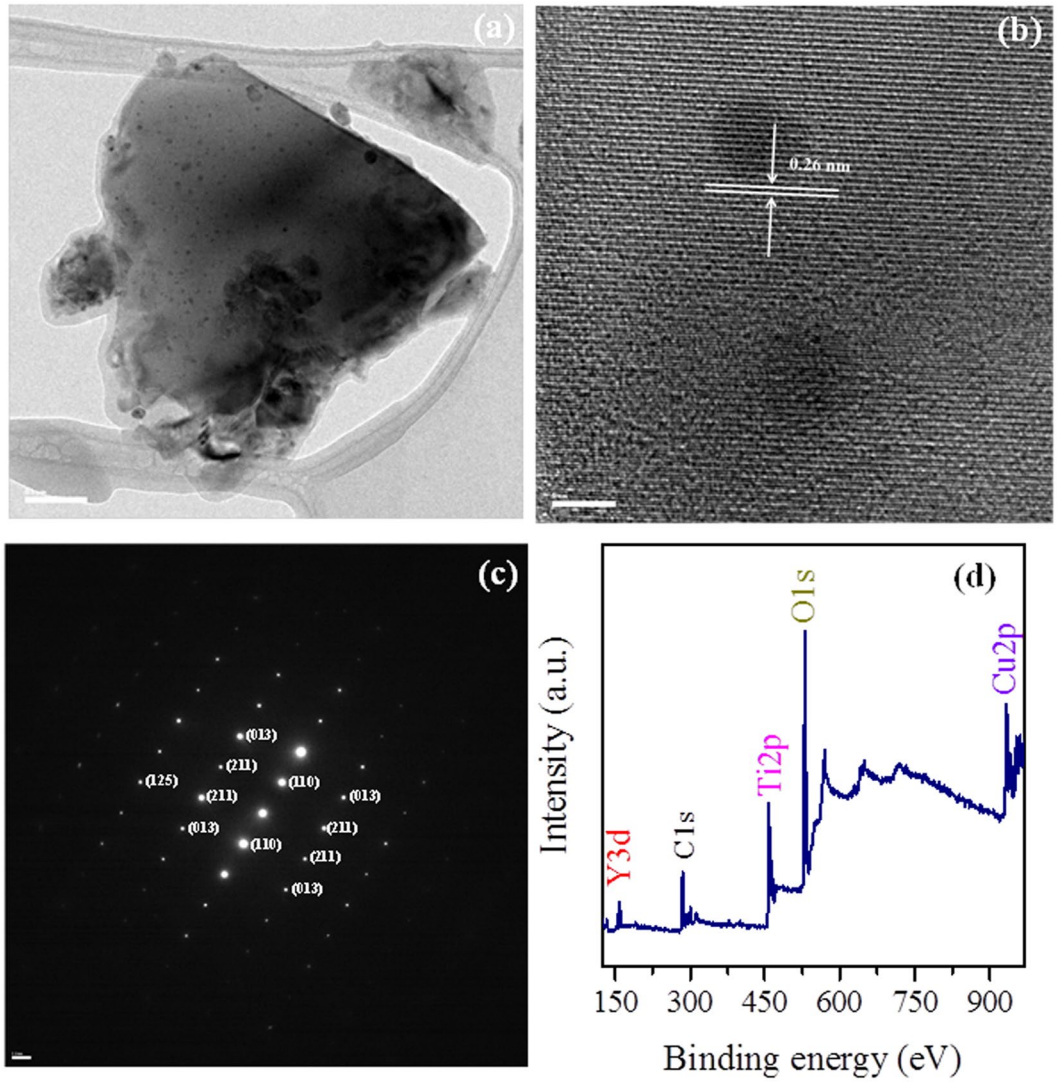


**Figure 3.** (**a**) TEM image, (**b**) HRTEM lattice image, (**c**) SAED pattern, and (**d**) XPS survey spectrum of phase-pure YCTO.

Figure 2(d) presents the Raman scattering spectrum, in which three main peaks are observed in the wave region of 400–600 $cm^{-1}$. The Raman peaks at 433 and 519 $cm^{-1}$ have the $A_g$ symmetry of $TiO_6$ rotation. The peak at 581 $cm^{-1}$ was assigned to the mode of $F_g$ symmetry of O–Ti–O anti-stretching. All three peaks assigned in the Raman spectrum have also been reported for isostructural CCTO perovskite[31].

High resolution transmission electronic microscopy (HRTEM) and selected area electron diffraction (SAED) of the auto flame synthesized YCTO powder were carried out to examine the crystallinity and phase-purity further. Figure 3(a) shows a TEM image of a YCTO particle. The HRTEM image of YCTO in Fig. 3(b) shows a typical lattice fringe indicating well-crystallized YCTO particles with interplanar spacing of 0.26 nm, corresponding to the (220) crystal planes and agreed well with the XRD data for the cubic perovskite phase. The SAED pattern as shown in Fig. 3(c) has a highly symmetrical dotted lattice, which supports the highly crystalline nature of YCTO. The diffraction spots of the SAED pattern were indexed to the (211), (013), (110), and (125) reflections of the cubic phase with space group *Im*3. X-ray photoelectron spectroscopy (XPS) was carried out to determine the compositions and oxidation state of the elements present in the YCTO powder and estimate the quality of material preparation. The detailed oxidation states with the XPS fitting parameter of each element are given in supplementary information S4. As shown in Fig. 3(d), the XPS survey spectrum showed the elemental peaks of Y, Cu, Ti, and O, which is consistent with the results of EDX characterization (see supplementary information S5). The unavoidable existence of a carbon peak (C 1 s) is due to adventitious carbon species.

**Characterization by cyclic voltammetry.** Figure 4(a) shows the cyclic voltammogram of the prepared composite material immobilized onto the GC electrode (GC/YCTO) in 0.1 M $H_2SO_4$, in which clear oxidation peaks were observed for $Cu^{2+}$ and $Y^{3+}$. A clear reduction peak was observed for Y, whereas no reduction peak was observed for Cu. According to a literature survey, this is the first report of the electrochemical properties of the prepared composite material. A detailed electrochemical study was performed to obtain greater insight.

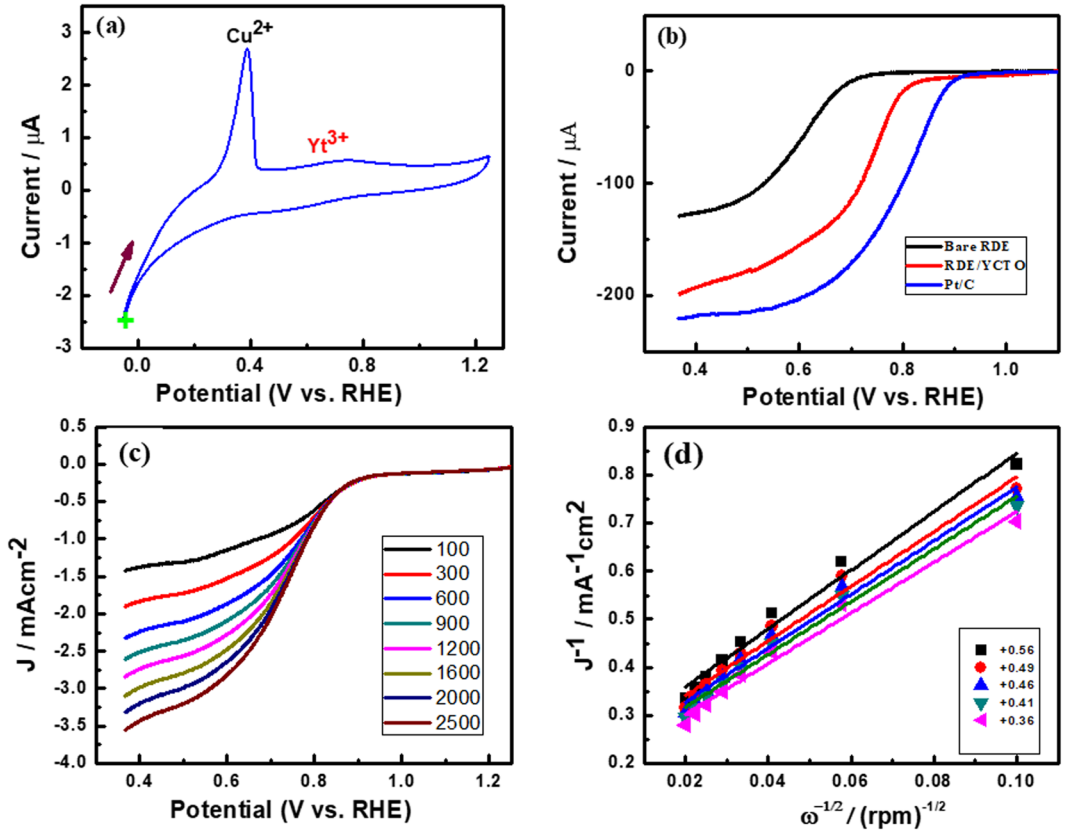


**Figure 4.** (**a**) Cyclic voltammogram of GC/Cu-Y in 0.1 M $H_2SO_4$ at a scan rate of 20 mV $s^{-1}$. The initial point of the scan is indicated by + sign. (**b**) Linear sweep voltammograms of bare RDE and RDE/Cu-Y and RDE/Pt/C at constant rotation speed in 0.1 M KOH at 10 mV $s^{-1}$ scan rate. (**c**) LSVs of the GC/Cu-Y electrode in $O_2$-saturated 0.1 M KOH solution at a scan rate of 10 mV $s^{-1}$ using RDE with different rotation (100, 300, 600, 900, 1200, 1600, 2000, and 2500 rpm). (**d**) Corresponding K-L plots of the ORR at different potentials, +0.56, +0.49, +0.46, +0.41, and +0.36 V.

**Electrocatalytic reduction of oxygen.** Figure 4(b) shows the linear sweep voltammogram of bare RDE and RDE/YCTO and RDE/Pt/C electrode at constant rotation speed in an oxygen saturated 0.1 M KOH solution at 10 mV $s^{-1}$ scan rate. At bare RDE reduction of oxygen begins at +0.71 V, whereas at RDE/YCTO and Pt/C it begins at +0.84 and 0.93 V respectively. Thus, reduction of oxygen at RDE/YCTO takes place 130 mV more positive and 90 mV less positive as compared to bare RDE and Pt/C respectively. Current density at RDE/YCTO is approximately 2 times higher as compared to bare RDE but less than Pt/C. This shows that the active sites on prepared composite materials are not well-defined as those on the Pt surface.

To examine the electron transfer kinetics of GC/YCTO during $O_2$ reduction, a hydrodynamic voltammetry study was carried out using RDE in an $O_2$ saturated 0.1 M KOH solution at different rotation speeds from 100 to 2,500 rpm, as shown in Fig. 4(c). The linear sweep voltammograms were recorded in an $O_2$ saturated 0.1 M KOH electrolyte at a scan rate of 10 mV $s^{-1}$ using a RDE. The measured current intensities for the modified electrode showed improvement with increasing rotating rate due to the enhanced diffusion of oxygen from solution to the electrode surface. In contrast, the LSVs of the GC/YCTO electrode revealed a direct four-electron transfer pathway for $O_2$ reduction. Very few reports are available for $O_2$ reduction using Cu as a catalyst, and there are no reports of YCTO for $O_2$ reduction.

Figure 4(d) shows the Koutecky-Levich plots of $J^{-1}$ vs. $\omega^{-1/2}$ at various potentials to determine the kinetic parameters of GC/YCTO. The kinetic parameters were calculated based on the Koutecky-Levich equations. The number of electrons transferred (n) in the ORR process for GC/YCTO electrode was calculated using the following Koutecky-Levich equation (1) [32]

$$\frac{1}{J} = \frac{1}{J_K} + \frac{1}{B\omega^{1/2}}$$
$$B = 0.62nFD_{O2}^{2/3}\nu^{-1/6}C_{O2} \quad (1)$$

Where F is the Faraday constant (96,500 C $mol^{-1}$), $D_{O2}$ is the diffusion coefficient of $O_2$ in a 0.1 M KOH aqueous solution ($1.9 \times 10^{-5}$ $cm^2$ $s^{-1}$), $\nu$ is the kinematic viscosity of the solution ($1.0 \times 10^{-2}$ $cm^2$ $s^{-1}$), and $C_{O2}$ is the oxygen concentration ($1.2 \times 10^{-6}$ M) in $O_2$ saturated solutions (0.1 M KOH). The slopes of the corresponding

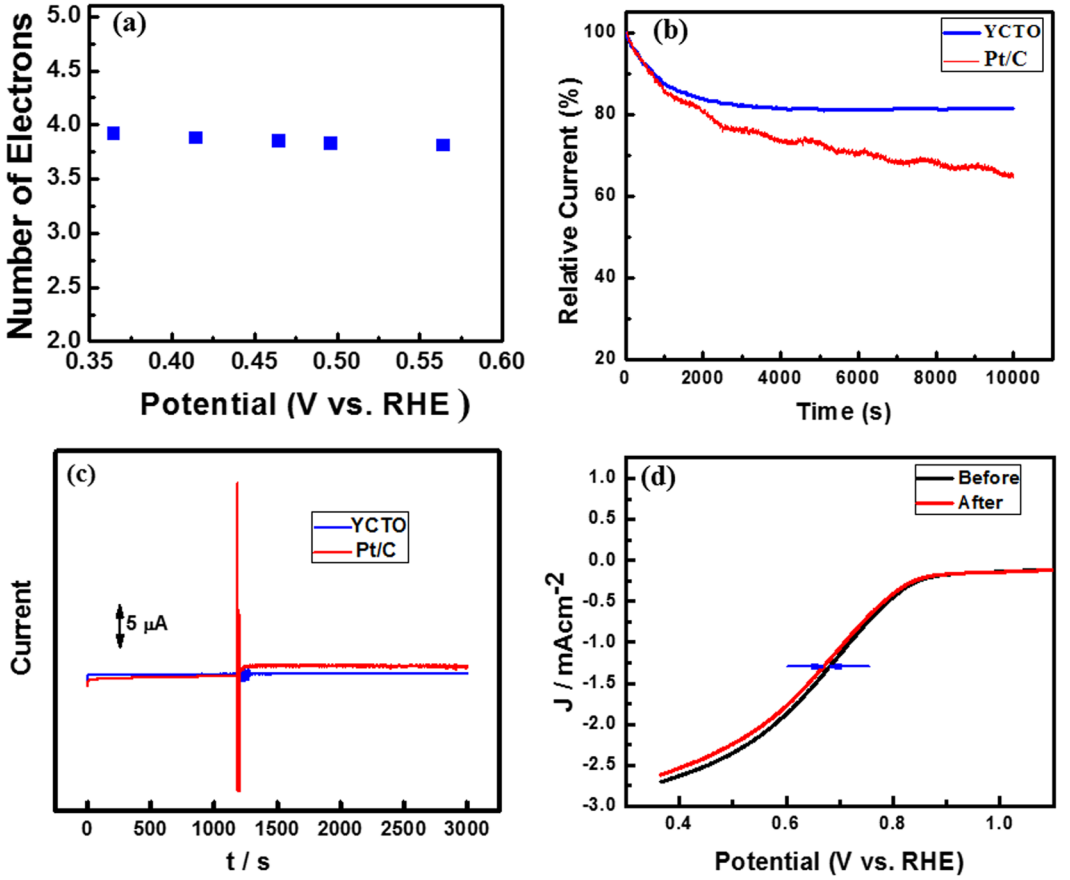


**Figure 5.** (**a**) Number of electrons transferred vs. the potential as calculated from the KL plots. (**b**) Relative current vs. time responses at −0.2 V in $O_2$-saturated 0.1 M KOH solution for GC/Cu-Y and 20 wt.% GC/Pt/C electrodes. (**c**) Chronoamperometric response of GC/Cu-Y and Pt/C at +0.60 V in oxygen saturated 0.1 M KOH followed by the addition of 3.0 M methanol. (**d**) Linear sweep curves of the ORR on the GC/Cu-Y electrode before and after 10,000 cycles in $O_2$-saturated 0.1 M KOH at 25 °C.

Koutecky-Levich plots ($J^{-1}$ *vs.* $\omega^{-1/2}$) at different reduction potentials are almost parallel and close to that of the calculated line for the four-electron reduction of oxygen in Fig. 5(a). The non-zero intercepts of the extrapolated Koutecky-Levich lines suggest that the $O_2$ reduction process on GC/YCTO is under mixed kinetic-diffusion control in a large potential range. The linearity and parallelism of the plots are considered typical of first-order reaction kinetics with respect to the concentration of dissolved $O_2$. As shown in Fig. 4(d), the Koutecky-Levich plots of $J^{-1}$ vs. $\omega^{-1/2}$ at potentials of +0.56, +0.49, +0.46, +0.41, and +0.36 V on GC/YCTO showed good linearity. From the slope (1/B) of the Koutecky-Levich plots, the n values for GC/YCTO at various potentials were calculated according to the above mentioned formula and were very close to four. Figure 5(a) shows the corresponding plots of the n values versus the potential. The number of electrons involved in the ORR was close to 4 at all potentials, indicating that reduction proceeds predominantly through a kinetically favorable pathway of direct conversion from $O_2$ to $OH^-$, as reported for noble metals, such as Pt, Pd, Ag-Au alloys, etc. refs 33, 34. As most of these types of ceramic materials are used in solid oxide fuel cells, the total number of electrons involved and the onset potential of the prepared composite is comparable to previously studies, as listed in Table 1 [35–48]. There are very few reports are available for such kinds of material synthesized via sol-gel technique. Hu *et al.* prepared $La_{1-x}Ca_{x}MnO_3$ perovskite-graphene composites and used for oxygen reduction[49]. However, they have neither studied the stability and poisoning of the material nor compared the performance with commercially available Pt/C catalysts.

Durability and tolerance is another important aspect of fuel cell catalysts that must be considered during the construction of a fuel cell. The chronoamperometric measurements of GC/YCTO and GC/Pt/C were carried out at 0.6 V for 10,000 s, as shown in Fig. 5(b). The 20% current loss in the initial current for GC/YCTO was observed, while approximately 36% loss of the initial current for GC/Pt/C was noted. This indicates that the GC/YCTO catalyst has much better durability than the commercial available Pt/C. The obtained stability is comparable to previously reported literature[50–52]. The GC/YCTO electrode was subjected to further testing to determine the possible crossover and stability toward the ORR. To examine the possible crossover effect in the presence of other fuel molecules (e.g., methanol), the current vs. time chronoamperometric responses for the ORR at the GC/YCTO and GC/Pt/C electrodes were measured, as shown in Fig. 5(c). A sharp positive and negative current change was observed for the Pt/C electrode upon the addition of 3.0 M methanol. On the other hand, the corresponding amperometric response for the GC/YCTO electrode remained almost unchanged even after the addition of

| Catalysts | Onset Potential (V) RHE | Peak Potential(V) | N | References |
|---|---|---|---|---|
| N-doped carbon frameworks | 0.79 | — | 3.95 | 35 |
| N-doped hollow fibers | 0.75 | 0.77 | 3.6 | 36 |
| ZIF-derived porous carbon | 0.83 | 0.68 | 3.3 | 37 |
| sulphur-doped graphene | 0.88 | 0.69 | 3.13 | 38 |
| N-CNT frameworks | 0.97 | 0.87 | 3.97 | 39 |
| Ordered mesoporous carbon | 0.81 | — | 3.1 | 40 |
| $Co_3O_4$/graphene Sheets | 0.88 | 0.84 | 3.9 | 41 |
| Co,N-CNF | 0.882 | — | — | 42 |
| Co/graphene Sheets | 0.80 | — | — | 43 |
| $LaCu_{0.5}Mn_{0.5}O_3$ | 0.80 | — | ≈4 | 44 |
| $La_{0.5}Sr_{0.5}CoO_{2.91}$ | ≈0.75 | — | 3.1 | 45 |
| $BaMnO_3$ | −0.19 (Ag/AgCl) | — | 3.4–3.7 | 46 |
| $LaFe_{0.95}Pd_{0.05}O_3$ | ≈−0.2 (Ag/AgCl) | | 3.94 | 47 |
| $La_{0.5}Sr_{0.5}Co_{0.8}Fe_{0.2}O_3$ | ≈0.9 | | 3.9–4 | 48 |
| $Y_{2/3}Cu_3Ti_4O_{12}$ | 0.84 | 0.7 | ≈4 | Present Work |

**Table 1.** Comparison of the ORR performance of the electrocatalyst reported earlier.

| Electrocatalyst | Number of Cycles | Changes in $E_{1/2}$ (mV) | References |
|---|---|---|---|
| P-Z8-Te-1000 | 8000 | 11 | 53 |
| C-N-Co | 10000 | 9 | 54 |
| Co, N-CNF | 5000 | 10 | 55 |
| NT-G | 8000 | 11 | 56 |
| PANI-Fe-C | 10000 | 10 | 57 |
| $Y_{2/3}Cu_3Ti_4O_{12}$ | 10000 | 9 | Present Work |

**Table 2.** Comparison of the $E_{1/2}$ of various electrocatalyst for oxygen reduction reaction.

methanol. This clearly indicates that the GC/YCTO electrocatalyst has higher fuel selectivity toward the ORR than the commercial Pt/C electrocatalyst.

The electrochemical stability of the ORR electrocatalyst depends on the structural stability of the material. To gain further insight into the stability of the catalytic activity of the GC/YCTO electrocatalyst in the present investigation, linear sweep voltammetry was performed between potential windows of 0.36 to 1.36 V at a 10 mV $s^{-1}$ scan rate under oxygen purging. Figure 5(d) presents the linear sweep voltammograms of the GC/YCTO electrode before and after 10,000 continuous cycles in an $O_2$ saturated 0.1 M KOH solution at room temperature. After 10,000 continuous potential cycles, the half-wave potential $E_{1/2}$ of YCTO exhibited a negative shift of only 9 mV in Fig. 5(d), which is much lower than previously reported electrocatalysts for ORR. The changes in $E_{1/2}$ of various electrocatalyst after several cycles have been listed in Table 2 [43,53–56]. The current did not show a significant decrease after 10,000 continuous cycles, which demonstrates the excellent stability of the GC/YCTO electrode for ORR applications than the commercial Pt/C electrocatalyst. SEM images of YCTO coated on the GC disk were recorded before and after the stability test, but no distinguishable morphological change was observed (see supplementary information S6).

## Discussion

Pristine $Y_{2/3}Cu_3Ti_4O_{12}$ powder was synthesized in a single step at 950 °C for 15 h, which is relatively simple, rapid with short sintering duration as compared to other conventional synthesis routes. The confirmation of phase formation and the composition by different physiochemical characterization techniques such as XRD, IR, Raman, XPS, and EDX showed the fabrication of good quality of YCTO material. The present automatic flame synthesis procedure is rapid and facile for $Y_{2/3}Cu_3Ti_4O_{12}$ with the merits of simplicity, energy, and time saving. In future, it may be considered for the large scale production of isostructural $ACu_3Ti_4O_{12}$ (A = Cd, $Sm_{2/3}$, $Bi_{2/3}$, and $La_{2/3}$) perovskite. The electrochemical RDE analysis showed that the number of electrons transferred in ORR is close to 4, indicating that $Y_{2/3}Cu_3Ti_4O_{12}$ promotes the four electron transfer pathway. This study clearly showed that $Y_{2/3}Cu_3Ti_4O_{12}$ is a promising material as an excellent electrocatalyst with enhanced fuel tolerance selectivity, durability, and electrochemical stability as well as higher ORR activity compared to commercial Pt/C. In addition, the UV-visible study of YCTO revealed a direct transition at 1.8 eV for the visible light absorption, which should be considered as a third generation photocatalyst similar to the well-established isostructural $CaCu_3Ti_4O_{12}$ perovskite reported earlier. The energy band gap ($E_g$) is an important feature of $ABO_3$ type metal oxides, which determine their applications in photocatalysis, electrocatalytic activity, and optoelectronics. For this purpose, the optical characterization was carried out (see supplementary information S7) and supported the results of the

electrocatalytic activity of YCTO. A direct transition with an energy band gap ($E_g$) of 1.8 eV was determined from the UV-visible diffuse reflectance spectrum. Furthermore, the electrocatalytic ORR activity and photocatalytic of the $Y_{2/3}Cu_3Ti_4O_{12}$ perovskite were correlated with the covalent networking and broad diversity of A- and B-site transition metals[22]. The electrocatalytic activities of $ABO_3$-type perovskite are associated with the corner shared network of $TiO_6$ octahedron, which can facilitate electron transfer and oxygen transfer in the lattice[57]. In addition, the large atoms at the A-site of $ABO_3$ allow stabilization of the multiple valence states of B-site metal cation[58]. Overall, YCTO has great potential for the next generation ORR catalyst and photocatalyst.

## Methods

**Material synthesis.** $Y(NO_3)_3{\cdot}6H_2O$ (99.80%, Aldrich), $Cu(NO_3)_2{\cdot}3H_2O$ (99.0%, Junsei), $TiO_2$ (99.9%, Sigma Aldrich), and 2-methoxyethanol (99.0%, Alfa Aesar) were used to prepare the $Y_{2/3}Cu_3Ti_4O_{12}$ (YCTO). A stoichiometric amount of $Y(NO_3)_3{\cdot}6H_2O$ and $Cu(NO_3)_2{\cdot}3H_2O$ was dissolved in a minimum amount of 2-methoxyethanol. A stoichiometric amount of solid $TiO_2$ was added to the homogeneous metal nitrate solution of $Y^{3+}$ and $Cu^{2+}$, and sonicated for 10–15 min. The heterogeneous mixture of metal ions was formed and heated to 90–120 °C for 30–35 min on a hot plate using a magnetic stirrer to evaporate the organic solvent until self-ignition took place, which exhausted a large amount of gases with a greenish flame, and produced a fluffy mass of YCTO precursor powder within 15–20 s. Upon cooling, the resulting product was ground using pestle and mortar and sintered without a pre-calcination step at 950 and 1050 °C for 15 hrs in an electrical furnace.

**Material characterization.** Thermogravimetric (TG) and differential scanning calorimetry (DSC) measurements of the auto flame synthesized precursor powder were carried out on SDT Q600 thermal analyzer (TA Instruments) from room temperature to 1050 °C with 10 °C $min^{-1}$ in a nitrogen atmosphere. The crystalline structure of the precursor powder and sintered at 950 and 1050 °C for 15 hrs was determined by X-ray diffraction (XRD, Rigaku Ultima IV, Japan) using Cu Kα radiation. The crystallinity and composition of the YCTO powder were investigated by transmission electron microscopy (TEM, JEM-2100F, Jeol, Japan) and scanning electron microscopy (SEM, JEOL JSM6500F, Japan) attached to energy-dispersive X-ray spectroscopy analyzer for elemental analysis. X-ray photoelectron spectroscopy (XPS, Thermo Fisher Kα, USA) was performed to determine the oxidation state and composition of the synthesized material. The Fourier transform infrared (FT-IR, Shimadzu IRAffinity-1S, Japan) spectrum of YCTO was acquired using KBr pellets at a suitable composition from 400 to 1600 $cm^{-1}$. Raman spectra (resolution: 4 $cm^{-1}$) were collected by a Raman microscope equipped with a diode laser ($\lambda_{ex} = 785$ nm, power = 44 mW), a CCD detector, and a holographic grating (Kaiser Optical Inc., Ann Arbor, MI, USA). Each sample was positioned on a microscope stage and the laser beam was focused with an objective lens (10×/0.25 NA) to collect spectra.

**Electrochemical Measurements.** *Instrumentation.* The electrochemical experiments were performed with a CHI-660C (CH Instruments, USA) using a three-electrode system with GC (CH Instruments, area = 0.07 $cm^2$) or modified GC as working electrode, platinum wire as the counter electrode and Ag/AgCl as the reference electrode. Rotating disk electrode (RDE) voltammetry was conducted on a Pine Research Instrument (AFMSRCE, USA) modulated speed rotator. All electrochemical experiments were carried out at 20 °C, and the potentials were referenced to Ag/AgCl. The solutions were purged with $N_2$ or $O_2$ for 20–30 min before the electrochemical experiments. All potentials reported were referenced to the reversible hydrogen electrode (RHE) through a RHE calibration. Eq. 1 was used to convert the obtained potential (vs. Ag/AgCl) to the RHE.

$$E_{RHE} = E_{Ag/AgCl} + 0.059\,pH + E_{Ag/AgCl}{}^{0} \quad (E_{Ag/AgCl}{}^{0} = +0.199\,V) \tag{1}$$

**Preparation of Electrode (GC/Cu-Y).** Typically, 2 mg of the Cu-Y composite was dissolved in 1.0 mL of ethanol and sonicated for 30 min. Using a micropipette, 10 µL of this solution was dropped to coat onto the surface of the GC electrode and 20 µL at RDE, respectively, and dried for 30 min.

## References


1. Badwal, S. P. S. *et al.* Emerging electrochemical energy conversion and storage technologies. *Front. Chem.* **2**, 1–28 (2014).
2. Shao, M. Electrocatalysis in fuel cells. *Catalysts* **5**, 2115–2121 (2015).
3. Zhang, Y. *et al.* A facile synthesis of nitrogen doped highly porous carbon nanoplatelets: efficient catalysts for oxygen electroreduction. *Sci. Rep.* **7**, 43366–10 (2017).
4. Kim, O. H. *et al.* Facile and gram-scale synthesis of metal-free catalysts: toward realistic applications for fuel cells. *Sci. Rep.* **5**, 8376–8 (2015).
5. Hong, J. W. *et al.* Controlled synthesis of Pd-Pt alloy hollow nanostructures with enhanced catalytic activities for oxygen reduction. *ACS Nano* **6**, 2410–2419 (2012).
6. Zhang, L., Iyyamperumal, R., Yancey, D. F., Crooks, R. M. & Henkelman, G. Design of Pt-shell nanoparticles with alloy cores for the oxygen reduction reaction. *ACS Nano* **7**, 9168–9172 (2013).
7. Wang, M. *et al.* Mesoporous hollow PtCu nanoparticles for electrocatalytic oxygen reduction reaction. *J. Mater. Chem. A* **1**, 2391–2394 (2013).
8. Tiwari, J. N. *et al.* Interconnected Pt-nanodendrite/DNA/reduced-graphene-oxide hybrid showing remarkable oxygen reduction activity and stability. *ACS Nano* **7**, 9223–9231 (2013).
9. Zhang, S., Shao, Y., Yin, G. & Lin, Y. Recent progress in nanostructured electrocatalysts for PEM fuel cells. *J. Mater. Chem. A* **1**, 4631–4641 (2013).
10. Zhang, J. & Li, C. M. Nanoporous metals: Fabrication strategies and advanced electrochemical applications in catalysis, sensing and energy systems. *Chem. Soc. Rev.* **41**, 7016–7031 (2012).
11. Yang, H. B. *et al.* Identification of catalytic sites for oxygen reduction and oxygen evolution in N-doped graphene materials: Development of highly efficient metal-free bifunctional electrocatalyst. *Sci. Adv.* **2**, 1501122–11 (2016).

12. Narayan, S. R., Manohar, A. K. & Mukerjee, S. Bi-functional oxygen electrodes – challenges and prospects. *Electrochem. Soc. Interface* **24**, 65–69 (2015).
13. Singh, L., Rai, U. S., Mandal, K. D. & Singh, N. B. Progress in the growth of $CaCu_3Ti_4O_{12}$ and related functional dielectric perovskites. *Prog. Cryst. Growth Charact. Mater.* **60**, 15–62 (2014).
14. Rai, U. S., Singh, L., Mandal, K. D. & Singh, N. B. An overview on recent developments in the synthesis, characterization and properties of high dielectric constant calcium copper titanate nano-particles. *Nanosci. Technol.* **1**, 1–17 (2014).
15. Savinell, R. F. Picking perovskites. *Nat. Chem.* **3**, 501–502 (2015).
16. Miyahara, Y., Miyazaki, K., Fukutsuka, T. & Ab, T. Catalytic roles of perovskite oxides in electrochemical oxygen reactions in alkaline media. *J. Electrochem. Soc.* **161**, F694–F697 (2014).
17. Huang, K. An emerging platform for electrocatalysis: perovskite exsolution. *Sci. Bull.* **61**, 1783–1784 (2016).
18. Pen, M. A. & Fierro, J. L. G. Chemical structures and performance of perovskite oxides. *Chem. Rev.* **101**, 1981–2017 (2001).
19. Bockris, J. O. 'M. & Otagawa, T. The electrocatalysis of oxygen evolution on perovskites. *J. Electrochem. Soc.* **131**, 290–302 (1984).
20. Suntivich, J. *et al*. Design principles for oxygen-reduction activityon perovskite oxide catalysts for fuel cells and metal–air batteries. *Nat. Chem.* **3**, 546–550 (2011).
21. Matsumoto, Y., Yoneyama, H. & Tamura, H. Influence of the nature of the conduction band of transition metal oxides on catalytic activity for oxygen reduction. *J. Electroanal. Chem. Interfacial Electrochem.* **83**, 237–243 (1977).
22. Yagi, S. *et al*. Covalency-reinforced oxygen evolution reactioncatalyst. *Nat. Comm.* **6**, 8249–6 (2015).
23. Chen, X. *et al*. Platinized graphene/ceramics nano-sandwiched architectures and electrodes with outstanding performance for PEM fuel cells. *Sci. Rep.* **5**, 16246–10 (2015).
24. Mathur, A., Kushwaha, H. S., Vaish, R. & Halder, A. Enhanced electrocatalytic performance of perovskite supported iron oxide nanoparticles for oxygen reduction reaction. *RSC Adv.* **6**, 94826–94832 (2016).
25. Clark, J. H. *et al*. Visible light photo-oxidation of model pollutants using $CaCu_3Ti_4O_{12}$: An experimental and theoretical study of optical properties, electronic structure, and selectivity. *J. Am. Chem. Soc.* **133**, 1016–1032 (2011).
26. Kushwaha, H. S. *et al*. Efficient solar energy conversion using $CaCu_3Ti_4O_{12}$photoanode for photocatalysis and photoelectrocatalysis. *Sci. Rep.* **6**, 18557–10 (2016).
27. Miyahara, Y., Miyazaki, K., Fukutsuka, T. & Abe, T. Catalytic roles of perovskite oxides in electrochemical oxygen reactions in alkaline media. *J. Electrochem. Soc.* **161**, F694–F697 (2014).
28. Carvajal, R. & Fullprof, J. Laboratory Leon Brillouin CEA-CNRSCEA/ Saclay, 91191 Gif sur Yvette Cedex, France, Version (2015).
29. Ng, W. W., Suh, J. & Kaduk, J. A. X-ray reference patterns and structure of the perovskite-related phase $R_2Cu_9Ti_{12}O_{36}$ (R = lanthanides). *Powder Diffr.* **20**, 193–197 (2005).
30. Thomazini, D., Gelfuso, M. V. & Volpi, G. M. S. Conventional and microwave-assisted sintering of $CaCu_3Ti_4O_{12}$ ceramics obtained from coprecipitated Powders. *Int. J. Appl. Ceram.Technol.* **12**, E73–E81 (2015).
31. Singh, L. *et al*. Dielectric studies of a nano-crystalline $CaCu_{2.90}Zn_{0.10}Ti_4O_{12}$ electro-ceramic by one pot glycine assisted synthesis from inexpensive $TiO_2$ for energy storage capacitors. *RSC Adv.* **4**, 52770–52784 (2014).
32. Jahan, M., Bao, Q. L. & Loh, K. P. Electrocatalytically active graphene-porphyrin MOF composite for oxygen reduction reaction. *J. Am. Chem. Soc.* **134**, 6707–6713 (2012).
33. Genies, L., Faure, R. & Durad, R. Electrochemical reduction of oxygen on platinum nanoparticles in alkaline media. *Electrochim. Acta* **44**, 1317–1327 (1998).
34. Tarasevich, M. R., Sadkowski, A. & Yeager, E. Comprehensive treatise of electrochemistry: oxygen electrochemistry. Plenum press, New York, **7**, 369 (1983).
35. Liang, H. W., Wei, W., Wu, Z. S., Feng, X. & Müllen, K. Mesoporous metal-nitrogen-doped carbon electrocatalysts for highly efficient oxygen reduction reaction. *J. Am. Chem. Soc.* **135**, 16002–16005 (2013).
36. Zhang, W., Wu, Z. Y., Jiang, H. L. & Yu, S. H. Nanowire-directed templating synthesis of metal-organic framework nanofibers and their derived porous doped carbon nanofibers for enhanced electrocatalysis. *J. Am. Chem. Soc.* **136**, 14385–14388 (2014).
37. Aijaz, A., Fujiwara, N. & Xu, Q. From metal-organic framework to nitrogen-decorated nanoporous carbons: high $CO_2$ uptake and efficient catalytic oxygen reduction. *J. Am. Chem. Soc.* **136**, 6790–6793 (2014).
38. Ma, Z., Dou, S., Shen, A., Tao, L. & Dai, L. Sulfur-doped graphene derived from cycled lithium sulfur batteries as a metal-free electrocatalyst for the oxygen reduction reaction. *Angew. Chem. Int. Ed.* **54**, 1888–1892 (2015).
39. Xia, B. Y. *et al*. A metal-organic framework-derived bifunctional oxygen electrocatalyst. *Nat. Energy* **1**, 15006–8 (2016).
40. Lee, S. *et al*. Designing a highly active metal-free oxygen reduction catalyst in membrane electrode assemblies for alkaline fuel cells: Effects of pore size and doping-site position. *Angew. Chem. Int. Ed.* **54**, 9230–9234 (2015).
41. Liang, Y. *et al*. $Co_3O_4$ nanocrystals on graphene as a synergistic catalyst for oxygen reduction reaction. *Nat. Mater.* **10**, 780–786 (2011).
42. Shang, L. *et al*. Well-dispersed ZIF-derived Co, N-Co-doped carbon nano frames through mesoporous-silica-protected calcination as efficient oxygen reduction electrocatalysts. *Adv. Mater.* **28**, 1668–1674 (2016).
43. Wu, G., More, K. L., Johnston, C. M. & Zelenay, P. High-performance electrocatalysts for oxygen reduction derived from polyaniline, iron, and cobalt. *Science* **332**, 443–447 (2011).
44. Suntivich, J. *et al*. Design principles for oxygen-reduction activity on perovskite oxide catalysts for fuel cells and metal–air batteries. *Nat.Chem.* **3**, 546–550 (2011).
45. Zhao, Y. *et al*. Hierarchical mesoporous perovskite $La_{0.5}Sr_{0.5}CoO_{2.91}$ nanowires with ultrahigh capacity for Li-air batteries. *PNAS* **109**, 19569–19574 (2012).
46. Xu, Y. *et al*. Carbon-coated perovskite $BaMnO_3$ porous nanorods with enhanced electrocatalytic properties for oxygen reduction and oxygen evolution. *Electrochim. Acta* **174**, 551–556 (2015).
47. Zhu, Y. *et al*. Boosting oxygen reduction reaction activity of palladium by stabilizing Its unusual oxidation states in perovskite. *Chem. Mater.* **27**, 3048–3054 (2015).
48. Park, H. W. *et al*. Electrospun porous nanorod perovskite oxide/nitrogen-doped graphene composite as a bi-functional catalyst for metal air batteries. *Nano Eng.* **10**, 192–200 (2014).
49. Hu, J., Wang, L., Shi, L. & Huang, H. Preparation of $La_{1-x}Ca_xMnO_3$ perovskite-graphene composites as oxygen reduction reaction electrocatalyst in alkaline medium. *J. Power Sources* **269**, 145–151 (2014).
50. Chen, P. *et al*. Nitrogen-doped nanoporous carbon nanosheets derived from plant biomass: an efficient catalyst for oxygen reduction reaction. *Energy Environ. Sci.* **7**, 4095–4103 (2014).
51. Wang, Z. L. *et al*. Gelatin-derived sustainable carbon-based functional materials for energy conversion and storage with controllability of structure and component. *Sci. Adv.* **1**, 1400035–9 (2015).
52. Li, J. C. *et al*. A 3D bi-functional porous N-doped carbon microtube sponge electrocatalyst for oxygen reduction and oxygen evolution reactions. *Energy Environ. Sci.* **9**, 3079–3084 (2016).
53. Zhang, W., Wu, Z. Y., Jiang, H. L. & Yu, S. H. Nanowire-directed templating synthesis of metal–organic framework nanofibers and their derived porous doped carbon nanofibers for enhanced electrocatalysis. *J. Am. Chem. Soc.* **136**, 14385–14388 (2014).
54. Liang, H. W., Wei, W., Wu, Z. S., Feng, X. & Mullen, K. Mesoporous metal–nitrogen-doped carbon electrocatalysts for highly efficient oxygen reduction reaction. *J. Am. Chem. Soc.* **135**, 16002–16005 (2013).
55. Shang, L. *et al*. Well-dispersed ZIF-derived Co,N-Co-doped carbon nanoframes through mesoporous-silica-protected calcination as efficient oxygen reduction electrocatalysts. *Adv. Mater.* **28**, 1668–1674 (2016).

56. Li, Y. *et al*. An oxygen reduction electrocatalyst based on carbon nanotube–graphene complexes. *Nat. Nanotech.* **7**, 394–400 (2012).
57. Moreira, M. L. *et al*. Structural and optical properties of $CaTiO_3$ perovskite-based materials obtained by microwave-assisted hydrothermal synthesis: An experimental and theoretical insight. *Acta Mater.* **57**, 5174–5185 (2009).
58. Chambers, S. A. *et al*. Instability, intermixing and electronic structure at the epitaxial $LaAlO_3/SrTiO_3$(001) heterojunction. *Surf. Sci. Rep.* **65**, 317–352 (2010).

## Acknowledgements

This study was supported by the National Research Foundation (NRF-2015R1D1A3A01019167 for Y. Lee and NRF-2015R1D1A4A01019630 for L. Singh) and Priority Research Centers Program (NRF-2009-0093818) funded by the Ministry of Education in the Republic of Korea.

## Author Contributions

Dr. L. Singh and Prof. Y. Lee designed the research work. The material synthesized characterized by Prof. Y. Lee and Dr. L. Singh. Electrochemical measurements and analyses carried out by U.P. Azad and V. Ganesan. Structural analyses was carried out by S.P. Singh. Analyses of the results were done by Prof. Y. Lee and Dr. L. Singh. The manuscript was written by Prof. Y. Lee, Dr. L. Singh U.P. Azad and U.S. Rai.

## Additional Information

**Supplementary information** accompanies this paper at doi:10.1038/s41598-017-09661-9

**Competing Interests:** The authors declare that they have no competing interests.

**Publisher's note:** Springer Nature remains neutral with regard to jurisdictional claims in published maps and institutional affiliations.

**Open Access** This article is licensed under a Creative Commons Attribution 4.0 International License, which permits use, sharing, adaptation, distribution and reproduction in any medium or format, as long as you give appropriate credit to the original author(s) and the source, provide a link to the Creative Commons license, and indicate if changes were made. The images or other third party material in this article are included in the article's Creative Commons license, unless indicated otherwise in a credit line to the material. If material is not included in the article's Creative Commons license and your intended use is not permitted by statutory regulation or exceeds the permitted use, you will need to obtain permission directly from the copyright holder. To view a copy of this license, visit http://creativecommons.org/licenses/by/4.0/.

© The Author(s) 2017